

Original paper

Calcium-rich dravite from the Arignac Gypsum Mine, France: Implications for tourmaline development in a sulfate-rich, highly magnesian meta-evaporite

Barbara DUTROW, Darrell HENRY

Department of Geology and Geophysics, Louisiana State University, Baton Rouge, Louisiana 70808 United States of America; dutrow@lsu.edu



Tourmaline occurs in a wide range of compositional environments, but its occurrence in meta-evaporites is less commonly investigated. Highly magnesian ($X_{\text{Mg}} = 0.90\text{--}0.98$), poikiloblastic tourmaline occurs in a sulfate-rich, anhydrite-gypsum-bearing meta-evaporite in the Arignac Gypsum Mine, France and preserves a petrologic record of this unusual geochemical environment. Originally a Triassic evaporite deposit, the sample is interpreted to have undergone high-temperature–low-pressure (HT–LP) metamorphism and subsequently experienced low-grade, highly deformed overprints. Poikiloblastic tourmaline preserves relicts of the HT–LP mineral assemblage, as inclusions of anhydrite, phlogopite, dolomite, tremolite, Cl-rich scapolite (71–85 % marialite component), rutile, zircon, and fluor-apatite. The low-grade deformational overprints are characterized by partial replacement of anhydrite by gypsum, phlogopite by clinocllore, dolomite by talc, and scapolite by mixtures of near end-member albite and K-feldspar with later crosscutting calcite and celestite. Tourmaline develops two textural zones – zone 1 with few mineral inclusions and zone 2 with abundant inclusions and/or complex chemical zoning.

The tourmaline is mostly dravite or Ca-rich (> 0.25 apfu Ca) dravite with a few analyses of oxy-dravite and one attaining a high-Ti composition consistent with the hypothetical species “magnesio-dutrowite”. The average zone-1 tourmaline has an ordered structural formula of $(\text{Na}_{0.61}\text{Ca}_{0.32}\square_{0.07})(\text{Mg}_{2.82}\text{Fe}^{3+}_{0.11}\text{Ti}_{0.06})(\text{Al}_{5.87}\text{Fe}^{3+}_{0.13})(\text{Si}_{5.93}\text{Al}_{0.07})(\text{BO}_3)_3(\text{OH})_3(\text{OH}_{0.51}\text{O}_{0.41}\text{F}_{0.07})$ and the average zone-2 tourmaline has an ordered structural formula of $(\text{Na}_{0.72}\text{Ca}_{0.21}\square_{0.07})(\text{Mg}_{2.80}\text{Ti}_{0.20})(\text{Al}_{5.76}\text{Fe}^{3+}_{0.17}\text{Mg}_{0.07})(\text{Si}_{5.91}\text{Al}_{0.09})(\text{BO}_3)_3(\text{OH})_3(\text{OH}_{0.57}\text{O}_{0.39}\text{F}_{0.04})$. Inter- and intragranular chemical variability observed in the tourmaline is primarily consistent with the operation of combinations of the $(\text{CaMg})(\text{NaAl})_{-1}$, $(\text{R}^{3+}\text{O})[\text{R}^{2+}(\text{OH})]_{-1}$ and $(\text{TiO}_2)[\text{R}^{2+}(\text{OH})_2]_{-1}$ exchange vectors.

Assuming 600 °C for tourmaline formation, the Na-Ca contents of the X-site yield fluid composition estimates of $\text{Na}^{+}_{\text{fluid}}$ of 480 mM and $\text{Ca}^{2+}_{\text{fluid}}$ of 160 mM for average zone-1 and $\text{Na}^{+}_{\text{fluid}}$ of 460 mM and $\text{Ca}^{2+}_{\text{fluid}}$ of 110 mM for average zone-2. Na is comparable to modern seawater, with Ca increased at least ten times. Partition coefficients involving aqueous fluids in equilibrium with tourmaline suggest that the dissolved constituents of the coexisting aqueous fluid were 144.7 ppm B, 3.0 ppm Cr, 8.6 ppm Mn and 53.6 ppm Ti for zone 1 compared to 145.4 ppm B, 0.7 ppm Cr, 13.6 ppm Mn and 16.6 ppm Ti for zone 2. Comparison of the Arignac tourmaline data with other meta-evaporites and sulfate- or scapolite-bearing lithologies demonstrate the remarkable commonalities and a few differences exhibited by tourmalines of these lithologies. These data contribute to our understanding of Mg-rich tourmaline formation and coexisting fluid compositions, require a modification of the AFM host rock compositional fields, and underscore the breadth of environments in which tourmaline forms.

Keywords: tourmaline supergroup, gypsum, anhydrite, dravite, magnesian, meta-evaporites

Received: 21 March 2022; **accepted:** 19 August 2022; **handling editor:** J. Cempirek

The online version of this article (doi: 10.3190/jgeosci.352) contains supplementary electronic material.

1. Introduction

Tourmaline supergroup minerals are extraordinary recorders of their petrologic environment (e.g., Henry and Dutrow 1996; Dutrow and Henry 2011; van Hinsberg et al. 2011a, 2011b). Not only is tourmaline stable throughout most thermal and baric conditions of the crust and upper mantle, but it is also stable across an extensive spectrum of chemical environments found in a wide range of rock types. These rock types range from common pegmatites and metapelites to unusual rocks such as highly

magnesium meta-ultramafic rocks and meta-evaporites. As such, tourmaline is widely used as a provenance indicator of host-rock composition. This relationship was originally illustrated using a simple Al–Fe–Mg (AFM) ternary diagram that related tourmaline compositions to eight host rock environments (Fig. 1; e.g., Henry and Guidotti 1985; Henry and Dutrow 2018). For most of the diagram, these host lithologies are relatively distinct, but the magnesian region of the original AFM diagram was the most problematic, with limited tourmaline compositional data and overlaps among possible rock types.

Although relatively uncommon, highly magnesium tourmalines ($X_{Mg} > 0.9$) are documented in a variety of host-rock lithologies, including magnesian metasediments ($\pm Cr, V$), calc-silicate rocks, metacarbonate rocks, magnesian skarns, meta-ultramafic rocks (metapyroxenites, low-Ca meta-ultramafic rock), and evaporites/meta-evaporites (e.g., Schreyer et al. 1980; Ayuso and Brown 1984; Henry and Guidotti 1985; Schertl et al. 1991; Modreski et al. 1997; Henry et al. 1999, 2008; Uher et al. 2002; Pertlik et al. 2003; Moore et al. 2004; Aleksandrov and Troneva 2006; Arif et al. 2010; Bačík et al. 2011, 2012; Belley et al. 2014; Adlakha and Hattori 2016; Warren 2016; Marger et al. 2019; Dutrow and Henry 2021). In the original Henry and Guidotti (1985) AFM diagram, three locally overlapping source-rock fields were distinguished for the highly magnesian portion of the diagram. These rock types (fields) are: metacarbonates/metapyroxenites, magnesian low-Al metapelites and metapsammities, and low-Ca ultramafics/Cr-, V-metasediments (Fig. 1). Clearly, the fields of tourmaline-bearing magnesian lithologies can be further refined with the addition of tourmaline chemical data from a wider variety of Mg-rich lithologies (e.g., Dutrow and Henry 2021).

Among the lithologies that contain highly magnesian tourmaline, meta-evaporites are noteworthy because, in addition to crystallizing over a large range of thermal and baric conditions, tourmaline is uniquely positioned to preserve evidence of this complex and ephemeral geologic system. These lithologies originate as sedimentary evaporitic sequences that commonly contain abundant halite with subordinate amounts of sulfate minerals (including anhydrite and gypsum), bittern salts, Ca- and

Na-carbonate minerals, borate minerals, as well as intercalated siliciclastic materials (e.g., Henry et al. 2008; Warren 2016). With the onset of diagenesis and metamorphism, many significant changes occur in evaporite sequences. Halite readily interacts with aqueous fluids to produce highly saline fluids that strongly interact with the local siliceous interbeds to generate calc-silicate lithologies. Original sedimentary minerals, such as calcite, dolomite, and other carbonate minerals, transform into marbles. Some metamorphosed evaporites contain albite- and microcline-bearing pseudomorphs after evaporitic mineral porphyroblasts (e.g., Na-carbonates, borates, and sulfates) and Cl-rich scapolite porphyroblasts (Henry et al. 2008). Subsequently, widely varying meta-evaporitic lithologies can further react with infiltrated fluids to form a wide range of meta-evaporite rocks with distinctive minerals such as highly magnesian silicate minerals (e.g., tourmaline, phlogopite, diopside, tremolite, talc, clinocllore), Na–Ca silicate minerals (e.g., scapolite, plagioclase), carbonate minerals (e.g., calcite, dolomite, magnesite) and/or sulfate minerals (e.g., anhydrite, gypsum) (Warren 2016).

Tourmaline is not restricted to a single meta-evaporitic lithologic type but occurs in a wide range of lithologies associated with meta-evaporites. Tourmaline has been found in meta-evaporitic rocks that include calcite marbles (e.g., Dutrow and Henry 2021), magnesite marbles (Barbosa et al. 2000), whiteschists of presumed evaporitic origin (e.g., Schreyer et al. 1980), calc-silicate rocks (e.g., Bačík et al. 2011, 2012), some varieties of tourmalinites (e.g., Slack et al. 1984; Henry et al. 2008), banded albite–phlogopite rocks and albitites (e.g., Riehl and Cabral 2018). Such a range for tourmaline occurrence is

likely related to the abundance of boron in evaporitic sequences and its high fluid mobility in and near these sequences. Table 1 gives the most common tourmaline species associated with meta-evaporitic lithologies (e.g., Henry and Dutrow 2018; Henry and Dutrow 2021).

Tourmalines associated with sulfate-dominant meta-evaporitic lithologies have not been previously investigated. While

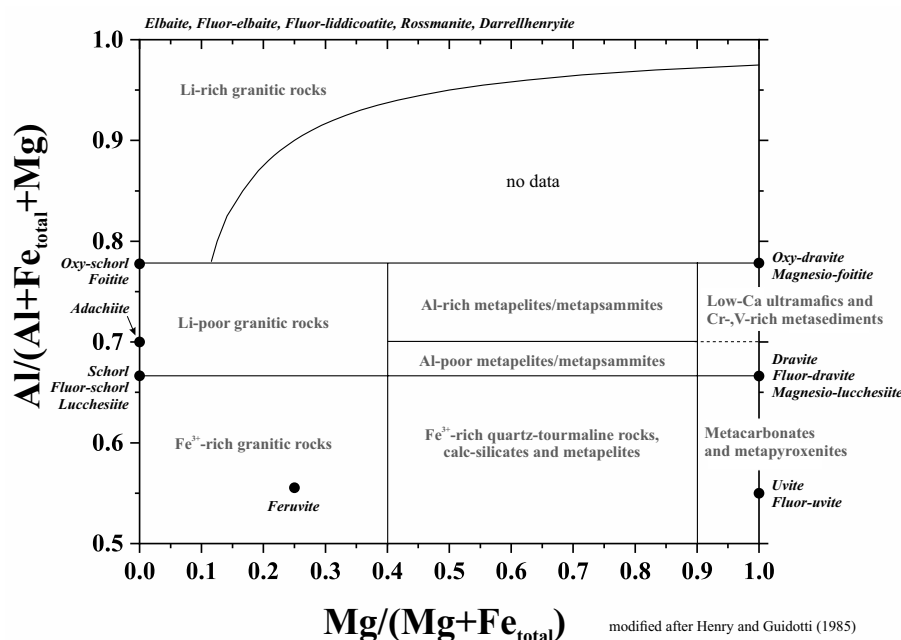


Fig. 1 Diagram correlating tourmaline compositions with source-rock type within the Al–Fe–Mg subsystem. This binary representation, redefined by Henry and Dutrow (2018), uses the original Henry and Guidotti (1985) data to delineate the rock-type boundaries. Italicized names represent compositions of select tourmaline end-member species.

Tab. 1 Important tourmaline species or components associated with meta-evaporitic lithologies

General formula:	(X)	(Y ₃)	(Z ₆)	T ₆ O ₁₈	(BO ₃) ₃	(V) ₃	(W)
Dravite	Na	Mg ₃	Al ₆	Si ₆ O ₁₈	(BO ₃) ₃	(OH) ₃	(OH)
Oxy-dravite	Na	Al ₂ Mg	Al ₅ Mg	Si ₆ O ₁₈	(BO ₃) ₃	(OH) ₃	(O)
Povondraite	Na	Fe ³⁺ ₃	Fe ³⁺ ₄ Mg ₂	Si ₆ O ₁₈	(BO ₃) ₃	(OH) ₃	(O)
Bosiite	Na	Fe ³⁺ ₃	Al ₄ Mg ₂	Si ₆ O ₁₈	(BO ₃) ₃	(OH) ₃	(O)
“Magnesio-dutrowite”*	Na	Mg _{2.5} Ti _{0.5}	Al ₆	Si ₆ O ₁₈	(BO ₃) ₃	(OH) ₃	(O)
Uvite	Ca	Mg ₃	Al ₅ Mg	Si ₆ O ₁₈	(BO ₃) ₃	(OH) ₃	(OH)
Magnesio-lucchesiite	Ca	Mg ₃	Al ₆	Si ₆ O ₁₈	(BO ₃) ₃	(OH) ₃	(O)
Magnesio-foitite	□**	Mg ₂ Al	Al ₆	Si ₆ O ₁₈	(BO ₃) ₃	(OH) ₃	(OH)
“Oxy-magnesio-foitite”*	□	Al ₂ Mg	Al ₆	Si ₆ O ₁₈	(BO ₃) ₃	(OH) ₃	(O)

* – Hypothetical tourmaline species currently not recognized by the International Mineralogical Association’s Commission on New Minerals, Nomenclature and Classification (IMA-CNMNC) but hypothesized based on crystal chemistry.

** – Designates X-site vacancy.

anhydrite is stable at moderate-to-high grades of metamorphism, it is rarely found in surface sulfate-rich rocks due to nearly complete conversion to gypsum with hydration at low temperatures (Warren 2016). This paper focuses on the chemical characterization of tourmalines and coexisting minerals associated with gypsum and anhydrite from an unusual meta-evaporitic occurrence to define mineral associations related to different stages of development of the meta-evaporite, to characterize the chemistry and controlling substitutions of the tourmaline from this unusual environmental setting, and to relate these features to the overall petrologic evolution of the meta-evaporites. The sample is from the Arignac Gypsum Mine, Ariège, Pyrenees, France (M. Ambroise, personal communication). Because the sample was obtained from a mineral dealer, information on coexisting lithologies and its exact geologic occurrence can only be inferred.

2. Geological settings

The meta-evaporites from the Arignac locality originally formed as Triassic salt deposits (Lagabrielle et al. 2010, 2020). These deposits are interpreted to have subsequently served as the tectonic sole for crust-mantle detachment faulting of the Iberian and European plates exposing pieces of mantle peridotites near the northern Pyrenean fault (Lagabrielle et al. 2010, 2020). Although limited geologic information is available, mineral assemblages and textures record at least two metamorphic events. Cretaceous (110–85 Ma) detachment faulting resulted in extreme continental thinning and a concomitant high temperature–low pressure (HT–LP) metamorphism of the meta-evaporites. The evaporite complexes are now polymictic breccias with blocks of dolomitic marble, meta-serpentinite, and anhydrite-rich meta-evaporite set in a highly deformed, low-grade matrix with abundant gypsum (Lagabrielle et al. 2010). In addition to anhydrite and gypsum, the following minerals have been documented previously at this locality: actinolite, aragonite,

calcite, celestine, clinocllore, dravite, mirabilite, phlogopite, pyrite and scapolite (Descouens 1984; mindat.org). Conditions of the HT–LP metamorphism are estimated to be 500–600 °C and 3–4 kbar (Golberg and Leyreloup 1990; Clerc et al. 2015). Based on ⁴⁰Ar/³⁹Ar and K–Ar geochronology of amphibole in a gypsum-bearing sample and of phlogopite in a marble, respectively, HT–LP metamorphism likely took place at 107–109 Ma (Thiébaud et al. 1992; Clerc et al. 2015). The HT–LP blocks incorporated into a strongly deformed gypsum-bearing low-grade matrix must have developed at conditions below the gypsum to anhydrite transition (i.e., from 40 to 120 °C; e.g., Yamamoto and Kennedy 1969; Dai et al. 2017) and are likely associated with a compressional stage reflective of the Iberian and European plate closure.

3. Analytical methods

Optical and Backscattered Electron (BSE) imaging of a single thin section are used to establish chemical heterogeneity and zoning patterns in tourmaline, to serve as a guide for microanalyses and, when coupled with energy dispersive spectrometry (EDS), to identify the qualitative chemical characteristics of the associated minerals phases and mineral inclusions.

Major, minor and trace element mineral chemistry was obtained for tourmaline, scapolite, and feldspar with the JEOL 8230 electron microprobe in the Department of Geology & Geophysics’ Chevron Geomaterials Characterization Lab of the Shared Instrumentation Facility at Louisiana State University. Analytical conditions included an accelerating potential of 15 kV, a beam current of 15 nA, and an electron beam diameter of 5 μm. Numerous points per grain and several grains in the thin section were analyzed.

A variety of well-characterized minerals were used as analytical standards. Primary standards for tourmaline analysis include andalusite (Al), diopside (Ca, Mg, Si), fayalite (Fe), chromite (Cr), rutile (Ti), rhodonite (Mn),

willemite (Zn), jadeite (Na), sanidine (K), tugtupite (Cl) and fluorite (F). For feldspar and scapolite, a common set of primary standards includes albite (Na, Si), sanidine (K), diopside (Ca, Mg), hematite (Fe), rhodonite (Mn), barite (S), and tugtupite (Cl). Several well-characterized tourmaline, scapolite and feldspar grains served as secondary standards to ensure consistency among analytical sessions and correct any machine drift. Analytical precision is estimated to be ± 1 percent relative for the major elements and ± 5 % for the minor elements. Detection limits for minor and trace elements are provided in the tables of analytical data (Tabs 2, 3 and 4). Analytical points were selected to assess the range of chemical heterogeneity and to obtain evidence for substitutions related to the evolving chemical host-rock environment.

Tourmaline was analyzed and normalized using several assumptions and normalization procedures. Tourmaline was normalized based on 15 $Y+Z+T$ cations and arranged in an ordered formula (Henry et al. 2011) with the stoichiometric amount of B_2O_3 iteratively calculated to produce three B atoms. Because the tourmaline formed in the presence of the sulfate mineral anhydrite, an oxidizing environment is assumed, consistent with the stability of sulfate minerals. Thus, all Fe is assumed to be Fe^{3+} . This assumption was examined further by assessing the relevant controlling substitutions and is explained subsequently. Li contents in magnesian tourmalines are likely minimal and insignificant in the structural formula of tourmaline (e.g., Henry and Dutrow 1996; Pesquera et al. 2016). The amount of deprotonation in tourmaline

was calculated based on charge balance, allowing the W -site anionic occupancy by OH, F and O to be estimated using the procedures suggested by Henry et al. (2011). For descriptive purposes, the root names of tourmaline species may be prefixed by the “Ca-rich” designation to indicate occupancy of > 0.25 *apfu* Ca of the X -site. For comparison, X_{Mg} is calculated as molar $Mg/(Fe_{total} + Mg)$. Where it is instructive, the sum of the Y - and Z -site divalent cations (Mg, Mn, Zn, Fe^{2+}) are collectively termed R^{2+} and the sum of the Y - and Z -site trivalent cations (Al, Fe^{3+} , Cr^{3+}) are collectively termed R^{3+} (Henry et al. 2011). Because the Fe is considered ferric, it is not included in the R^{2+} sum.

Scapolite and feldspar analytical procedures are similar with differences in data normalization. The scapolite structural formula is calculated based on $Si+Al=12$ cations. The scapolite components marialite ($Na_4Al_3Si_9O_{24}Cl$), meionite ($Ca_4Al_6Si_6O_{24}CO_3$) and silvialite ($Ca_4Al_6Si_6O_{24}SO_4$) were calculated assuming marialite % = $100 * [Na/(Na+Ca)]$, meionite % = $100 * [Ca/(Ca+Na)] * [C/(C+S)]$ and silvialite % = $100 * [Ca/(Ca+Na)] * [S/(C+S)]$. Feldspars are normalized based on 8 O *apfu*.

4. Results

4.1. Mineralogical associations

Megascopically, the meta-evaporite sample consists of 1–4 mm dark-brown anhedral tourmaline grains and 1–3 mm pale brown phlogopite grains set in a fine-grained beige matrix consisting mostly of gypsum and anhydrite (Fig. 2). The identification and chemical characteristics of the minerals were verified with EDS.

Petrographically, two stages of metamorphism are recognized: (1) a relatively high-grade assemblage preserved as inclusions within the tourmaline porphyroblasts or as relict coarse grains in the matrix and (2) a low-grade overprint that is accompanied by significant deformation. Based on microanalytical studies, the high-grade metamorphic assemblage includes tourmaline, anhydrite, phlogopite, dolomite, tremolite, Cl-rich scapolite, with minor rutile, zircon, and fluor-apatite. Millimeter-sized scapolite grains occur as relicts in the matrix, whereas small scapolite grains occur as inclusions in tourmaline. Dolomite contains small inclusions of anhydrite, phlogopite, tremolite with rutile and zircon and is crosscut by celestine and Mg-bearing calcite. Albite, K-feldspar and celestine are found also as inclusions in tourmaline. Petrologic arguments suggest these are secondary and likely due to a thermal resetting associated with the low-grade overprint (see discussion). The low-grade overprint is manifest by partial-to-complete replacement of anhydrite by gypsum, phlogopite by clinocllore, dolomite by talc, and scapolite by mixtures

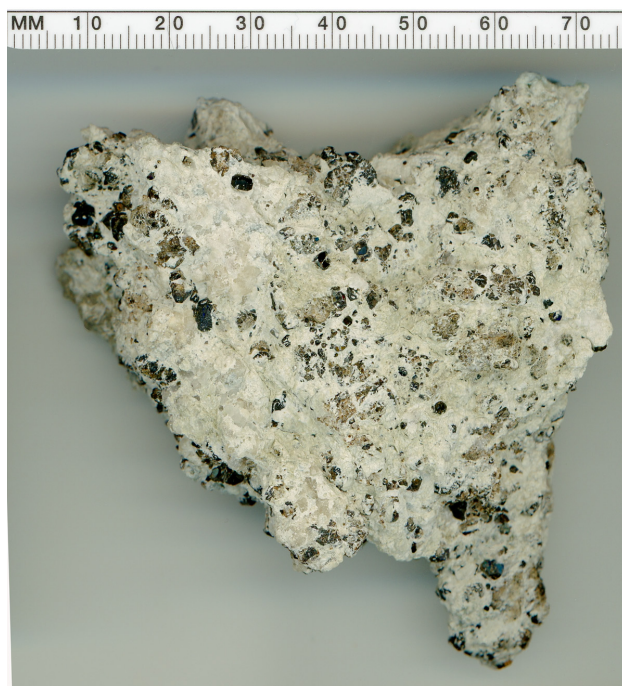


Fig. 2 Photograph of the hand sample of tourmaline-bearing gypsum-anhydrite meta-evaporitic rock with scale.

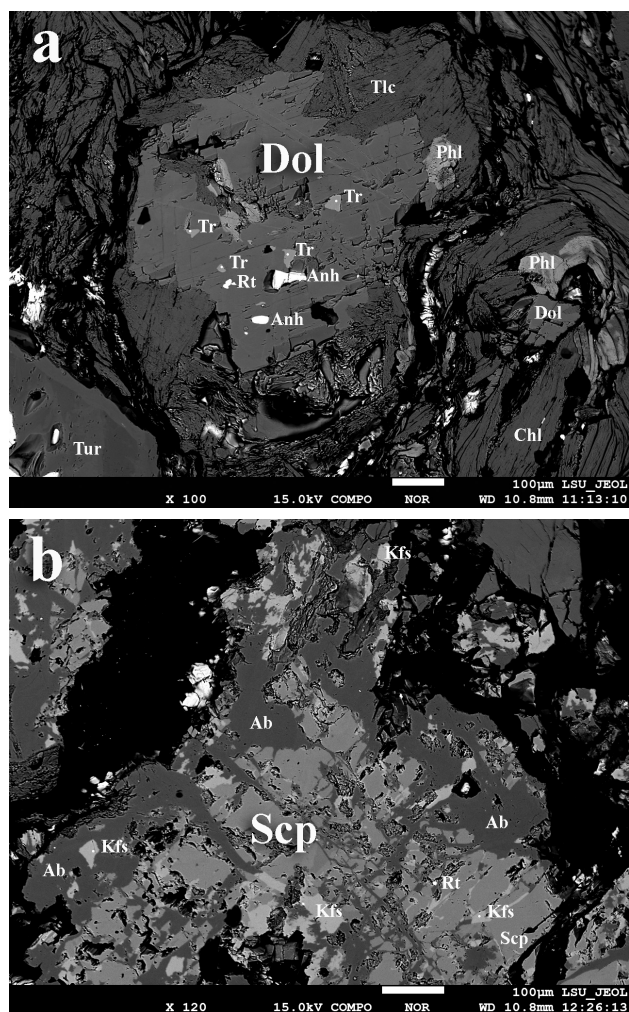


Fig. 3 BSE images of high-grade matrix minerals associated with the tourmaline, showing their high-grade mineral inclusions and partial replacement by lower-grade minerals. **a** – High-grade metamorphic dolomite (Dol) with included anhydrite (Anh), tremolite (Tr), phlogopite (Phl) and rutile (Rt). Deformed phlogopite is partially replaced by clinocllore (Chl) and dolomite by talc (Tlc). **b** – High-grade metamorphic scapolite (Scp) with inclusions of rutile. Scapolite is partially replaced by nearly pure albite (Ab) and K-feldspar (Kfs).

of albite and K-feldspar with later crosscutting calcite and celestite (Figs 3a, b). Alternatively, there may be two lower-grade overprints, a slightly higher-temperature event causing clinocllore to replace phlogopite and talc to replace dolomite, followed by a lower-grade event of gypsum replacing anhydrite.

Imaging reveals the textural relations of the minerals. Optically, tourmaline grains are pleochroic from pale orange to orange-brown with irregular color zoning and have sub-to-euhedral morphology. Parts of many of the grains are poikiloblastic with notable amounts of medium-grained (100–400 µm) subhedral inclusions of anhydrite. In addition, some grains are highly poikiloblastic tourmaline and commonly contain small (10–50 µm) anhedral inclusions of phlogopite, scapolite, tremolite,

rutile, and zircon (Fig. 4). Backscattered-electron imaging illustrates that some areas of tourmaline grains (here referred to as zone-1 regions) have few mineral inclusions and simple growth zoning and other areas (zone-2 regions) contain abundant small mineral inclusions and/or heterogeneous chemical zoning typical of tourmaline that overgrows and inherits the matrix texture (Dutrow et al. 2019, Fig. 4). Because the tourmaline inclusions relate to the high-grade assemblage, a discrete stage of tourmaline nucleation and growth is not observed related to the lower grade event e.g., small tourmaline crystals. Select minerals were chemically characterized to provide additional information.

4.2. Tourmaline, scapolite and feldspar chemical compositions

Electron microprobe data define the chemical characteristics of important silicate minerals in the meta-evaporite. Representative data are presented in Tabs 2, 3 and 4 and complete analytical data of these minerals are included in the Electronic Supplementary File (ESM 1).

4.2.1. Tourmaline

Five poikiloblastic grains were analyzed to define the range of tourmaline compositions in each of the two zones defined by inclusion density. All analyses fall within the alkali-group tourmaline field, i.e., Na+K = 0.54–0.83 *apfu*, Ca = 0.08–0.39 *apfu* and X-site vacancy = 0.03–0.14 (Fig. 5a). The average zone-1 tourmaline is

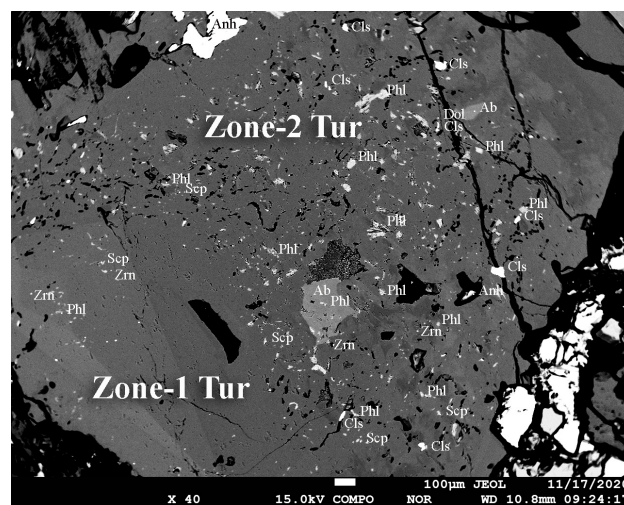


Fig. 4 High-grade tourmaline with an outer zone-1 inclusion-poor region and an inner zone-2 inclusion-rich region. The lighter gray bands on the left side of the zone-1 tourmaline is compositionally distinct from zone-2 tourmaline on the right side. Most inclusions appear to be part of the peak metamorphic assemblage, including scapolite, phlogopite, zircon (Zrn), and anhydrite. Albite and celestine (Cls) are interpreted to be retrograde minerals.

Tab. 2 Zone averages and selected tourmaline analyses for extremes in sample 19-FR-gyp

Tourmaline Zone	Zone 1	Zone 2	Zone 1	Zone 2	Zone 2	Zone 1	Zone 2	Zone 2
Analysis designation	Zone 1 avg.	Zone 2 avg.	Highest Ca	Lowest Ca	Highest Ti	Lowest Ti	Highest Al	Lowest Al
SiO ₂	36.91	36.60	36.56	36.63	37.01	37.08	36.65	35.86
TiO ₂	0.52	1.67	0.62	0.65	2.37	0.32	0.68	2.31
B ₂ O ₃ *	10.82	10.77	10.77	10.75	10.91	10.80	10.81	10.51
Al ₂ O ₃	31.36	30.76	30.94	31.44	30.82	31.69	32.51	28.90
Cr ₂ O ₃	0.01	0.04	0.00	0.03	0.06	0.01	0.03	0.01
Fe ₂ O ₃ **	2.00	1.41	2.19	1.61	1.30	1.84	0.45	1.43
MgO	11.79	11.90	11.96	11.62	12.07	11.52	11.68	12.08
MnO	0.01	0.00	0.00	0.00	0.00	0.00	0.00	0.00
ZnO	0.01	0.01	0.02	0.01	0.01	0.02	0.02	0.00
CaO	1.86	1.22	2.28	0.45	1.31	1.45	0.91	1.76
Na ₂ O	1.94	2.29	1.72	2.63	2.27	2.14	2.46	2.00
K ₂ O***	b.d.l.	b.d.l.	b.d.l.	0.01	b.d.l.	b.d.l.	b.d.l.	0.01
F	0.14	0.09	0.17	0.05	0.00	0.06	0.00	0.02
Cl	0.00	0.00	0.01	0.01	0.00	0.01	0.00	0.00
H ₂ O****	3.28	3.32	3.24	3.51	3.33	3.32	3.49	3.16
Subtotal	100.66	100.09	100.49	99.39	101.47	100.25	99.68	98.05
O=F	-0.06	-0.04	-0.07	-0.02	-0.00	-0.03	-0.00	-0.01
Total	100.60	100.06	100.41	99.37	101.47	100.23	99.68	98.04
Normalization based on 15 Y + Z + T cations – ordered formula								
B-site	B*	3.000	3.000	3.000	3.000	3.000	3.000	3.000
T-site	Si	5.930	5.906	5.898	5.924	5.897	5.965	5.927
	Al	0.070	0.094	0.102	0.076	0.103	0.035	0.073
Z-site	Al	5.869	5.756	5.780	5.918	5.685	5.973	6.000
	Cr ³⁺	0.001	0.005	0.000	0.004	0.007	0.001	0.001
	Fe ^{3+**}	0.130	0.171	0.220	0.078	0.155	0.026	0.178
	Mg	0.000	0.067	0.000	0.000	0.153	0.000	0.264
Y-site	Al	0.000	0.000	0.000	0.000	0.000	0.000	0.058
	Ti	0.063	0.203	0.075	0.079	0.284	0.039	0.288
	Cr ³⁺	0.000	0.000	0.000	0.000	0.000	0.000	0.004
	Fe ^{3+**}	0.111	0.000	0.046	0.118	0.000	0.197	0.000
	Mg	2.824	2.795	2.876	2.801	2.715	2.762	2.712
	Mn ²⁺	0.001	0.001	0.000	0.000	0.000	0.001	0.000
	Zn	0.001	0.001	0.003	0.002	0.001	0.002	0.000
X-site	Ca	0.321	0.211	0.394	0.079	0.224	0.249	0.311
	Na	0.606	0.717	0.539	0.826	0.701	0.666	0.641
	K	0.000	0.000	0.000	0.001	0.000	0.000	0.001
	vacancy	0.073	0.072	0.067	0.095	0.075	0.085	0.046
V-site	OH	3.000	3.000	3.000	3.000	3.000	3.000	3.000
W-site	OH	0.513	0.570	0.489	0.790	0.537	0.564	0.489
	F	0.072	0.045	0.087	0.023	0.000	0.031	0.008
	Cl	0.000	0.000	0.002	0.003	0.001	0.001	0.000
	O	0.414	0.385	0.421	0.184	0.462	0.404	0.503
Al (total)		5.938	5.850	5.882	5.994	5.788	6.008	5.630
Mg/(Fe _{tot} +Mg)		0.921	0.944	0.915	0.935	0.949	0.925	0.944
OH (V+W-site)		3.513	3.570	3.489	3.790	3.537	3.564	3.489
Species with prefix modifier	Ca-rich dravite	Dravite	Ca-rich dravite	Dravite	Dravite	Dravite	Dravite	Ca-rich "magnesian-dutrowite"

Minimum detection limits for minor and trace elements analyzed: Cr₂O₃ = 0.01 wt. %, MnO = 0.01 wt. %, ZnO = 0.01 wt. %, K₂O = 0.004 wt. % and Cl = 0.01 wt. %. B.d.l. – below detection limits.

* – B₂O₃ calculated assuming 3 B in the structural formula.

** – All Fe assumed to be Fe³⁺.

*** – Less than the detection limit.

**** – H₂O calculated based on charge balance.

more calcic than that of the average zone-2 tourmaline. However, there are two clusters of data in zone-1 compositions – one that is significantly more calcic (left side of zone-1 tourmaline in Fig. 4) and one that has Ca contents like zone-2 tourmaline (right portion of zone-1 tourmaline); these zones are apparent also in the BSE image (Fig. 4). The *W*-site anions fall mostly in the hydroxy-species field with 3 analyses plotting barely in the oxy-species field, all analyses are low in fluorine, i.e., ${}^w(\text{OH}) = 0.42\text{--}0.79$ apfu, ${}^w\text{O} = 0.11\text{--}0.53$ apfu and $\text{F} = 0.01\text{--}0.17$ (Fig. 5b). Aluminum contents are low-to-moderate with $\text{Al}_{\text{total}} = 5.63\text{--}6.16$ apfu. Titanium contents are substantial with $\text{Ti} = 0.04\text{--}0.28$ apfu. The average Ti value of zone-1 tourmaline is lower than zone-2 tourmaline. These high-Ti values are comparable to some of the higher Ti values found in tourmaline (e.g., Henry and Dutrow 1996). All tourmalines are highly magnesian with $\text{Mg}/(\text{Fe}_{\text{total}} + \text{Mg}) = 0.90\text{--}0.98$; the average zone-1 tourmaline is slightly less magnesian than average zone-2 tourmaline (Fig. 5c, d). Based on the analytical data, the tourmaline can be

classified as primarily dravite or Ca-rich (>0.25 apfu Ca) dravite. Two of the oxy-tourmaline analyses are Ca-rich oxy-dravite. One oxy-tourmaline analysis also contains >0.25 apfu Ti and ${}^y\text{Ti} > {}^y\text{Al}$, consistent with a hypothetical tourmaline species “magnesian-dutrowite” (Tab. 1).

4.2.2. Scapolite

Scapolite compositions are generally dominated by the Na-Cl marialite component ($>69\%$), with chemical variations reflective of the modes of occurrence of the scapolite, i.e., matrix relicts or inclusions (Tab. 3, supplemental Table). The coarser-grained matrix scapolite is homogeneous except for some irregular patches that appear to be relict regions partially replaced by the later-generation scapolite. The average later-generation matrix scapolite has components of 71.4 % marialite, 25.3 % meionite and 3.3 % silvialite and contrasts with the Na-Cl-richer earlier-generation matrix relicts having 84.3 % marialite, 13.2 % meionite and 2.5 % silvialite. The scapolite inclusions share many compositional similarities to the early- and late-stage matrix scapolite. The scapolite inclusions in zone-1 tourmaline are compositionally like the early-generation matrix scapolite and have an average composition of 85.4 % marialite, 11.2 % meionite and 3.4 % silvialite. In turn, the scapolite inclusions in

Tab. 3 Average scapolite compositions in different occurrences throughout 19-FR-gyp

Analysis area	1	2	3	4	5	
SiO ₂	55.46	59.17	55.67	54.64	59.99	
Al ₂ O ₃	22.59	20.77	22.61	22.98	20.69	
FeO	0.02	0.00	0.18	0.35	0.22	
CaO	7.01	3.95	6.96	7.39	3.74	
Na ₂ O	9.69	11.72	9.99	9.44	12.13	
K ₂ O	0.30	0.14	0.12	0.11	0.14	
Cl	3.27	3.78	3.22	3.11	3.88	
CO ₂ *	0.84	0.35	0.88	0.94	0.26	
SO ₃	0.20	0.12	0.27	0.35	0.14	
Subtotal	99.37	99.98	99.89	99.31	101.19	
O=Cl	-0.74	-0.85	-0.73	-0.70	-0.87	
Total	98.63	99.13	99.16	98.61	100.32	
Normalization based on Si + Al = 12						
<i>T</i> -site	Si	8.108	8.488	8.115	8.023	8.531
	Al	3.892	3.512	3.885	3.977	3.469
<i>M</i> -site	Fe ²⁺	0.003	0.000	0.022	0.043	0.026
	Ca	1.098	0.607	1.087	1.162	0.570
	Na	2.746	3.259	2.824	2.688	3.343
	K	0.055	0.025	0.021	0.021	0.025
<i>M</i> -site total		3.965	3.891	3.954	3.913	3.965
<i>A</i> -site	Cl	0.811	0.919	0.795	0.774	0.934
	C*	0.167	0.068	0.175	0.188	0.050
	S	0.022	0.013	0.030	0.039	0.015
<i>A</i> -site total		1.000	1.000	1.000	1.000	1.000
% Marialite		71.44	84.30	72.21	69.82	85.43
% Meionite		25.30	13.19	23.74	25.03	11.17
% Silvialite		3.26	2.51	4.05	5.14	3.40

Analysis area: 1 – Matrix scapolite; 2 – Relict in matrix scapolite; 3 – Inclusions in zone-2 tur – grain 1; 4 – Inclusions in zone-2 tur – grain 2; 5 – Inclusions in zone-1 tur – grain 2.

Minimum detection limits for minor and trace elements analyzed: FeO = 0.012 wt. %, MnO = 0.011 wt. %, MgO = 0.010 wt. %, K₂O = 0.008 wt. %, SO₃ = 0.005 wt. %. * – calculated.

Tab. 4 Average feldspar compositions in different occurrences throughout 19-FR-gyp

Analysis area	1	2	3	4	5	
SiO ₂	68.56	65.05	68.30	68.20	67.84	
Al ₂ O ₃	19.73	18.03	19.67	19.72	19.91	
FeO	0.08	0.00	0.13	0.24	0.20	
MgO	0.08	0.00	0.04	0.02	0.05	
CaO	0.04	0.02	0.06	0.03	0.25	
Na ₂ O	11.47	1.41	11.56	11.63	11.47	
K ₂ O	0.28	15.84	0.30	0.21	0.10	
Total	100.24	100.35	100.06	100.06	99.84	
Normalization based on 8 O apfu						
<i>T</i> -site	Si	2.989	3.000	2.986	2.982	2.972
	Al	1.014	0.980	1.013	1.016	1.028
<i>T</i> -site total		4.002	3.980	3.999	3.999	4.001
<i>M</i> -site	Fe ²⁺	0.003	0.000	0.005	0.009	0.007
	Mg	0.005	0.000	0.003	0.001	0.003
	Ca	0.002	0.001	0.003	0.002	0.012
	Na	0.969	0.126	0.980	0.986	0.974
	K	0.016	0.932	0.017	0.012	0.006
<i>M</i> -site total		0.987	1.059	0.999	0.999	0.992
% Albite		98.22	11.91	98.07	98.67	98.24
% Anorthite		0.21	0.07	0.27	0.16	1.18
% Orthoclase		1.57	88.02	1.65	1.17	0.58

Analysis area: 1 – Albite after matrix sep – grain 1; 2 – Kfs after matrix sep – grain 2; 3 – Pl after matrix sep – grain 2; 4 – Large pl inclusion in zone-2 tur; 5 – Pl inclusions in zone-2 tur. Minimum detection limits for minor and trace elements analyzed: FeO = 0.012 wt. %, MnO = 0.011 wt. %, MgO = 0.010 wt. %, K₂O = 0.008 wt. %.

the zone-2 portions of multiple tourmaline grains are more calcic like the later-formed matrix scapolite; their range of average compositions is 69.8–72.2 % marialite, 23.7–25.0 % meionite and 4.1–5.1 % silvialite.

4.2.3. Feldspar

Two types of feldspars occur in the sample: albite and K-feldspar. All occurrences of plagioclase feldspars are highly albitic ($Ab > 97\%$). The average composition of a relatively large inclusion in a zone-2 tourmaline is $Ab_{98.7}An_{0.2}Or_{1.2}$ (Fig. 4, Tab. 4, supplemental Table). The average composition of several small ($< 50\ \mu\text{m}$), isolated plagioclase inclusions in a zone-2 tourmaline is $Ab_{98.2}An_{1.2}Or_{0.6}$, like the composition of the larger plagioclase inclusion. In

the matrix, scapolite is partially pseudomorphed by albite with the range of average values $Ab_{98.1-98.2}An_{0.2-0.3}Or_{0.6-1.7}$. This albite is slightly more orthoclase rich than the plagioclase inclusions in tourmaline. A single K-feldspar analysis in an albite-K-feldspar partial pseudomorph after scapolite yielded a composition of $Ab_{11.9}An_{0.1}Or_{88.0}$.

5. Discussion

5.1. Petrogenetic evolution of the sulfate-rich meta-evaporite at the Arignac gypsum mine

The mineral assemblage and mineral chemistry in this sulfate-rich meta-evaporite sample are reflective of their

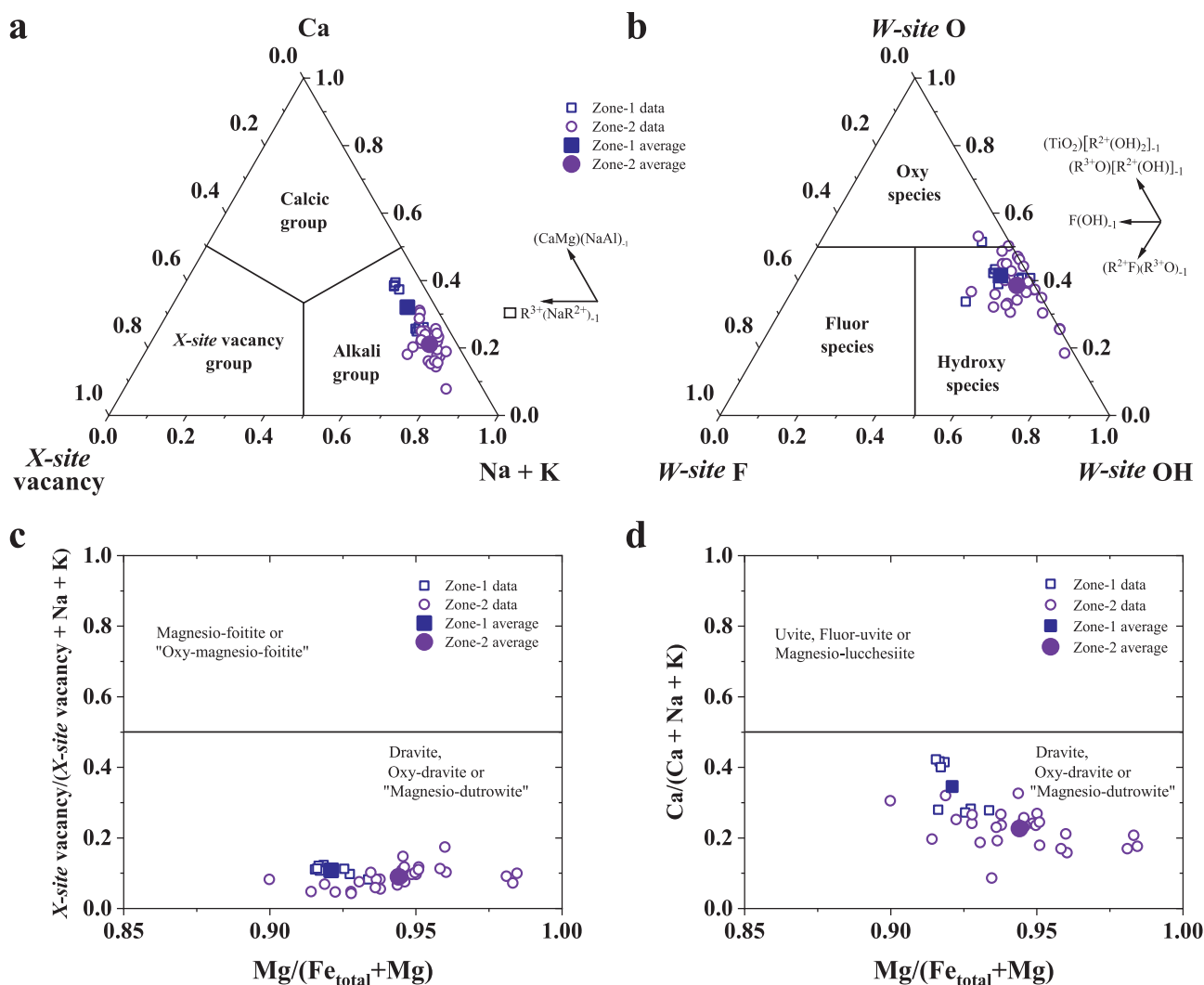


Fig. 5 Classification diagrams for primary and secondary tourmaline groups and possible tourmaline species. **a** – Primary tourmaline groups based on X -site occupancy. The labeled arrows represent the general directions of reference exchange vectors. **b** – Secondary tourmaline groups based on W -site anion occupancy (Henry et al. 2011). ${}^W\text{O}$ and ${}^W\text{(OH)}$ anions are calculated based on charge balance (see text for details). Applicable exchange vectors are shown by arrows. **c** – $\text{Mg}/(\text{Fe}_{\text{total}} + \text{Mg})$ vs. X -site vacancy/ $(X$ -site vacancy + $\text{Na} + \text{K})$ diagram. This diagram is valid for tourmalines that are not ${}^3\text{Ca}$ dominant (e.g., Henry and Dutrow 2001, 2012; Henry et al. 2002; Henry and de Brodtkorb 2009; Dutrow and Henry 2016). **d** – $\text{Mg}/(\text{Fe}_{\text{total}} + \text{Mg})$ vs. $\text{Ca}/(\text{Ca} + \text{Na} + \text{K})$ diagram. For **c** and **d**, specific species can be established by considering the dominant W -site anion and Ti contents.

pressure–temperature conditions, multiple metamorphic and fluid infiltration events, and their host lithology bulk composition. Protoliths of meta-evaporites are widely variable and typically contain various proportions of halite, anhydrite, gypsum, magnesian carbonates, bitters, borates, and siliciclastic clays (Warren 2016). Although specific P–T conditions cannot be directly calculated, several lines of evidence provide helpful information on general conditions.

Based on textural relations, the presumed high-grade metamorphic assemblage of tourmaline + anhydrite + phlogopite + dolomite + tremolite + marialite scapolite + rutile + zircon + fluor-apatite is consistent with meta-evaporites developed from a halite-, anhydrite-bearing protolith and metamorphosed at the presumed HT–LP conditions of the locality (e.g., Warren 2016). Crystallization of tourmaline in meta-evaporite rocks requires the presence of boron and acidic conditions. These conditions are commonly associated with the presence of evaporitic borate minerals or an influx of boron-bearing fluids (e.g., Henry et al. 2008; Warren 2016). While the resultant fluids must be acidic for tourmaline stability, fluids could be initially neutral or alkaline and become acidified when reacting with matrix minerals.

The formation of marialite likely reflects the halite and/or trona reacting with the siliciclastic clays during metamorphism. The other highly magnesian minerals are consistent with this type of occurrence. The two stages of scapolite development, from higher marialite component ($\sim \text{Ma}_{85}$) in the relict portion of the matrix scapolite and in the zone-1 inclusions, to lower marialite ($\sim \text{Ma}_{70}$) developed later, imply higher NaCl concentration in the earlier fluids (e.g., Vanko and Bishop 1982; Warren 2016). Experimental work on marialite suggests that high NaCl concentration and high temperature are necessary to stabilize the marialite end-member. However, the addition of even moderate amounts of meionite components (Me_{11-25}) significantly expands scapolite's stability to lower temperatures ($< 650^\circ\text{C}$) at low-to-moderate pressures (Almeida and Jenkins 2019). The changing scapolite compositions, from $\sim \text{Ma}_{85}$ to $\sim \text{Ma}_{70}$, suggest the later stage of scapolite formation occurred at lower temperatures and/or lower activity of NaCl in the fluids.

The low-grade metamorphic overprint could reflect a continuum of conditions rather than discrete heating episodes. Two-feldspar thermometry can be applied to this sample using the albite and orthoclase components of the coexisting albite and K-feldspar that partially replaces matrix scapolite. Calculations using different formulations for the two feldspars yield temperatures of $431/456^\circ\text{C}$ (Benisek et al. 2004), $410/439^\circ\text{C}$ (Benisek et al. 2010) and $456/457^\circ\text{C}$ (Putirka 2008) for assumed pressure conditions of 1 and 3 kbar. Although the calculated thermal conditions are out of the calibration range of the original thermometers, the convergence of the

calculated temperatures is petrologically reasonable for this replacement feature. Talc in dolomite-bearing rocks will form in H_2O -rich fluids at temperatures $< 450^\circ\text{C}$ assuming a pressure of 3–5 kbar (Bucher and Grapes 2011). This temperature is maximal for dolomite replacement by talc and is likely related to late hydrothermal activity in a retrograde overprint.

The transition of anhydrite to gypsum occurs at markedly lower temperatures ($< 200^\circ\text{C}$) and is accompanied by a $\sim 39\%$ volume increase (Kosztolanyi et al. 1987). Sulfate evaporites respond to differential stress, even at low temperatures, commonly resulting in foliation and flow in the evaporites that may lead to misinterpretation of primary bedding (Schreiber and Helman 2005). In the Arignac locality, relict high-grade anhydrite-rich meta-evaporitic blocks are set in a strongly sheared gypsum-rich matrix with a well-developed foliation and lineation (Lagabrielle et al. 2010). Deformation of the gypsum is observed directly in BSE images of the sample.

5.2. Tourmaline controlling substitutions and chemical evolution

Tourmaline chemical variations and attendant substitution mechanisms in the meta-evaporites of Arignac reflect the evolution of the bulk rock composition, the local coexisting mineral assemblage as thermal and baric changes occur, their mineral chemistries and the evolving fluid composition present during tourmaline poikiloblast formation. As protolith evaporites are heated, salts are mobilized and the fluid-rich environment alters its composition, becoming increasingly enriched in ions such as Na, Mg, Cl, SO_4 and BO_3 (e.g., Schreyer and Abraham 1976). During this strong metasomatic phase, tourmaline likely

Tab. 5 Possible site substitutions and corresponding exchange vectors for the Arignac tourmaline

Site substitution*	Exchange vector
${}^{1/2}\text{Fe}^{2+} = {}^{1/2}\text{Mg}$	MgFe_{-1}
${}^{1/2}\text{Al} = {}^{1/2}\text{Fe}^{3+}$	$\text{Fe}^{3+}\text{Al}_{-1}$
${}^{1/2}\text{R}^{2+**} + {}^w\text{OH}^- = {}^{1/2}\text{R}^{3+} + {}^w\text{O}^{2-}$	$(\text{R}^{3+}\text{O})[\text{R}^{2+}(\text{OH})]_{-1}$
${}^x\text{Na} + {}^{1/2}\text{Mg} = {}^x\text{Ca} + {}^{1/2}\text{Al}$	$(\text{CaAl})(\text{NaMg})_{-1}$
${}^x\text{Na} + {}^{1/2}\text{R}^{2+} = {}^x\text{Ca} + {}^{1/2}\text{R}^{3+}$	$(\text{CaR}^{3+})(\text{NaR}^{2+})_{-1}$
${}^x\text{Na} + {}^{1/2}\text{Al} = {}^x\text{Ca} + {}^{1/2}\text{Mg}$	$(\text{CaMg})(\text{NaAl})_{-1}$
${}^{1/2}\text{Mg} + {}^w\text{OH}^- = {}^{1/2}\text{Al} + {}^w\text{O}^{2-}$	$(\text{AlO})[\text{Mg}(\text{OH})]_{-1}$
${}^{1/2}\text{R} + {}^w\text{OH}^- = {}^{1/2}\text{Al} + {}^w\text{O}^{2-}$	$(\text{AlO})[\text{R}(\text{OH})]_{-1}$
${}^{1/2}\text{R}^{2+} + {}^w\text{F}^- = {}^{1/2}\text{R}^{3+} + {}^w\text{O}^{2-}$	$(\text{R}^{3+}\text{O})[\text{R}^{2+}(\text{F})]_{-1}$
${}^w\text{OH}^- = {}^w\text{F}^-$	$\text{F}(\text{OH})_{-1}$
${}^{1/2}\text{R}^{2+} + 2{}^w\text{OH}^- = {}^{1/2}\text{Ti} + 2{}^w\text{O}^{2-}$	$(\text{TiO}_2)[\text{R}^{2+}(\text{OH})_2]_{-1}$
$2\text{Al} = \text{Ti} + \text{R}^{2+}$	$(\text{TiR}^{2+})\text{Al}_{-2}$
${}^{1/2}\text{R}^{2+} + \text{Si} = {}^{1/2}\text{Al} + {}^t\text{Al}$	$({}^{1/2}\text{Al}^t\text{Al})(\text{R}^{2+}\text{Si})_{-1}$

* – Precursor italicized superscripts designate possible sites in tourmaline involved in a substitution.

** – R^{2+} represents the sum of divalent cations $\text{Fe}^{2+} + \text{Mg} + \text{Mn}$. R^{3+} represents the sum of trivalent cations $\text{Al} + \text{Fe}^{3+} + \text{Cr} + \text{V}$.

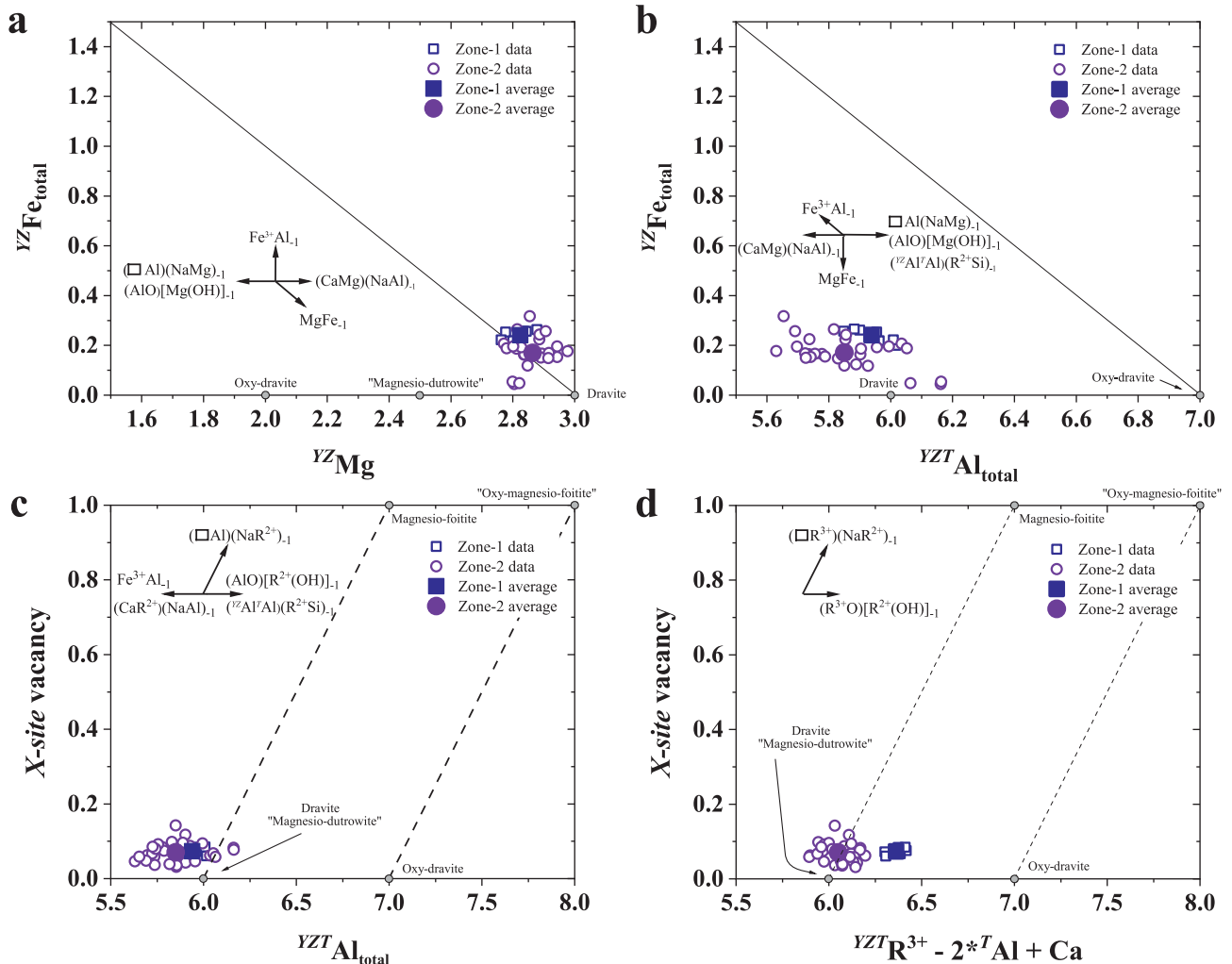


Fig. 6 Selected tourmaline binary diagrams used to constrain substitutions involving the X , Y , Z and T -sites. Diagonal lines refer to reference vectors, described for each diagram. **a** – $YZMg$ vs. $YZFe_{total}$ diagram. The oxidation state of Fe is unspecified. Arrows represent the directions of reference exchange vectors; the reference line is parallel to the $MgFe_{-1}$ exchange vector. **b** – $YZTAl_{total}$ vs. $YZFe_{total}$ diagram; reference line is parallel to the $Fe^{3+}Al_{-1}$ exchange vector. **c** – $YZTAl_{total}$ vs. X -site vacancy diagram; reference lines parallel to the $(\square Al)(NaR^{2+})_{-1}$ exchange vector and connect selected species locations. **d** – $YZTR^{3+} - 2 * TAl + Ca$ vs. X -site vacancy diagram. The X -axis term is the numerical projection parameter that accounts for the $(CaR^{2+})(NaAl)_{-1}$ and $(^{1/2}Al^{1/2}Al)(R^{2+}Si)_{-1}$ vectors. $YZTR^{3+}$ is the sum of the trivalent cations $YZTAl_{total} + Fe^{3+} + Cr + V$ on the Y , Z - and T -sites and YZR^{2+} is the sum of the divalent cations on the Y and Z sites, i.e., $Mg + Mn + Zn$.

formed. Once tourmaline formed, these external conditions exerted an influence on tourmaline compositions. By evaluating the operative substitutions in tourmaline through a series of ternary and binary diagrams (Tab. 5, Figs 5–7), speculation of the processes impacting their compositional evolution follows.

The predominant chemical constituents in the X - and W -sites not only define the tourmaline primary and secondary group (Fig. 5), but their variations constrain some of the controlling substitutions involving these two sites. Although all tourmalines are classified as alkali-group, there are substantial and variable amounts of Ca, i.e., 0.08–0.39 *apfu* (Fig. 5a, Tab. 2). Distribution of this data is mostly consistent with the operation of the $(CaMg)(NaAl)_{-1}$ exchange vector with a magnitude of up to ~ 0.3

apfu for the entire compositional range. For the W -site, if it is assumed that all Fe is Fe^{3+} , the variation of anions is primarily consistent with the operation of the $(R^{3+}O)[R^{2+}(OH)]_{-1}$ and/or $(TiO_2)[R^{2+}(OH)_2]_{-1}$ vectors up to 0.3 *apfu* with some dispersion into ternary space consistent with combinations of $F(OH)_{-1}$ and $(R^{2+}F)(AlO)_{-1}$ (Fig. 5b).

Consideration of cations on the Y - and Z -sites provides a more complete determination of the operative substitutions. A plot of ^{XY}Mg and $YZFe_{total}$ does not make assumptions about either the Y - or Z -site occupancy or the oxidation state of Fe (Fig. 6a). These data show there is no apparent systematic relationship between Mg and Fe (i.e., along a $MgFe_{-1}$ exchange vector) implying little or no Fe^{2+} and supporting the assumption of all Fe as Fe^{3+} for completing the charge balance calculations. The non-sys-

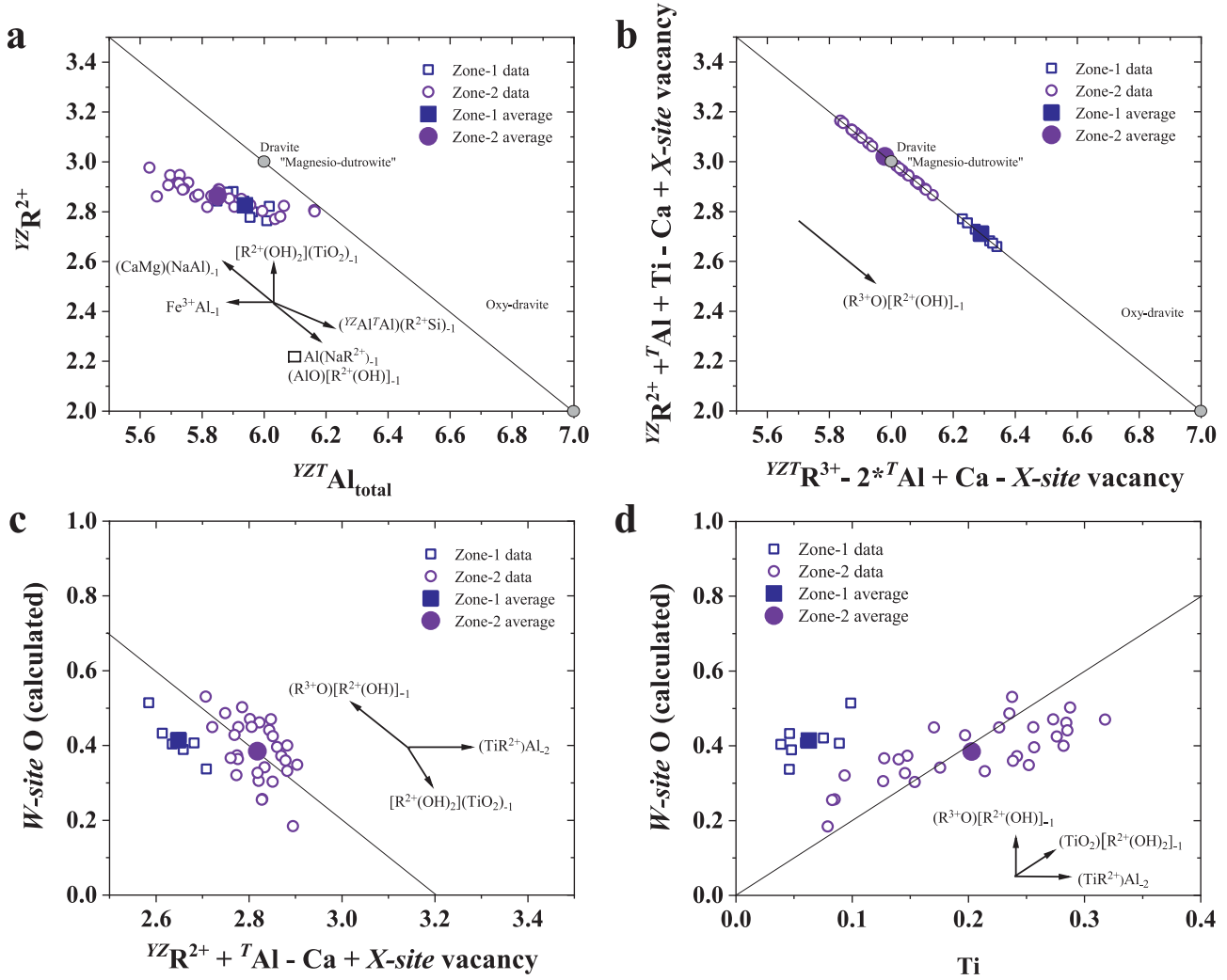


Fig. 7 Selected tourmaline binary diagrams used to constrain possible substitutions involving the X, Y, Z, T and W-sites. Diagonal lines refer to reference vectors, described for each diagram. **a** – $YZTAl_{total}$ vs. YZR^{2+} diagram. The data are in a general linear array deviating from the reference line consistent with $(CaMg)(NaAl)_{-1}$, $(Al)(NaR^{2+})_{-1}$ and $(AlO)[R^{2+}(OH)]_{-1}$ vectors. However, the data are influenced by other competing exchange vectors. **b** – $YZR^{2+} + TAl + Ca - X\text{-site vacancy}$ versus $YZR^{2+} + Ti + TAl - Ca + X\text{-site vacancy}$ diagram. These expressions in account for $(CaMg)(NaAl)_{-1}$, $[R^{2+}(OH)_2](TiO_2)_{-1}$, $Al(NaR^{2+})_{-1}$ and $(^YAl^TAl)(R^{2+}Si)_{-1}$ substitutions. **c** – $YZR^{2+} + TAl - Ca + X\text{-site vacancy}$ versus $W\text{-site O}$ diagram. The reference line is parallel to the $(R^{3+}O)[R^{2+}(OH)]_{-1}$ vector. **d** – Ti versus $W\text{-site O}$ diagram. The line is a linear fit of the zone-2 data constrained to intersect at the zero Y-intercept with a slope of 1.90 ± 0.14 ; an $r^2 = 0.84$ and is most compatible with the $(TiO_2)[R^{2+}(OH)_2]_{-1}$ vector.

tematic spread of the data is likely related to the operation of combinations of multiple exchange vectors illustrated in Fig. 6a. The $YZTAl_{total}$ versus $YZFe_{total}$ diagram exhibits a range in Al, up to 0.6 apfu with a slight inverse relation between Al and Fe (Fig. 6b). This range likely reflects the cumulative effects of the $Fe^{3+}Al_{-1}$ exchange vector combined with the Ca, oxy- and X-site vacancy-substitutions. The $YZTAl_{total}$ versus X-site vacancy diagram displays the small amount of X-site vacancy (typically $< 0.15 \text{ apfu}$) with the range in Al of up to 0.6 apfu (Fig. 6c). The horizontal dispersion of data ($5.6\text{--}6.2 \text{ apfu Al}$) is related to combinations of those exchange vectors that operate along a horizontal trend, noted on the diagram (Fig. 6b).

Within simple binary composition diagrams, substitutions involving components beyond those of the binary

system can be considered by projection down selected exchange vectors to the binary system (e.g., Henry and Dutrow 1990, 2001; Henry et al. 2002). For the $YZTAl_{total}$ versus X-site vacancy diagram, the diagram can be recast as $R^{3+} - 2TAl + Ca$ versus X-site vacancy (Fig. 6d); the former being a term that quantifies the influence of the $(^YAl^TAl)(R^{2+}Si)_{-1}$ and $(CaMg)(NaAl)_{-1}$ exchange vectors. This projection results in improved compositional clustering of the data in zones 1 and 2, respectively. The separation of these zones by an average of $\sim 0.25 \text{ apfu}$ is most consistent with the operation of the $(R^{3+}O)[R^{2+}(OH)]_{-1}$ vector. A similar relation occurs with the $YZTAl_{total}$ versus YZR^{2+} diagram, in which there is a general linear array of data that is influenced by a series of competing substitutions (Fig. 7a). To accommodate the possible competing

vectors, the data are recast as ${}^Y\text{R}^{3+} - 2\text{Al} + \text{Ca} - X\text{-site vacancy}$ versus ${}^Y\text{R}^{2+} + \text{Ti} + \text{Al} - \text{Ca} + X\text{-site vacancy}$ which corrects for the $(\text{CaR}^{2+})(\text{NaAl})_{-1}$, $(\square\text{Al})(\text{NaR}^{2+})_{-1}$, $[\text{R}^{2+}(\text{OH})_2](\text{TiO}_2)_{-1}$ and $({}^Y\text{Al}^T\text{Al})(\text{R}^{2+}\text{Si})_{-1}$ exchange vectors (Fig. 7b). As a consequence, data are arrayed on the diagonal parallel to the $(\text{R}^{3+}\text{O})[\text{R}^{2+}(\text{OH})]_{-1}$ vector. The zone-1 data (corrected R^{3+} 6.20–6.35 *apfu*) are clearly separated from the zone-2 data (corrected R^{3+} 5.80–6.15 *apfu*), implying that the inclusion-rich zone-2 compositions developed in less oxidizing conditions.

The reactions that likely control the incorporation of O into the *W*-site can be assessed with two additional binary diagrams. The ${}^Y\text{R}^{3+} + \text{Al} - \text{Ca} + X\text{-site vacancy}$ versus *W*-site O diagram accounts for the influence of the $(\text{CaR}^{2+})(\text{NaAl})_{-1}$, $(\square\text{Al})(\text{NaR}^{2+})_{-1}$ and $({}^Y\text{Al}^T\text{Al})(\text{R}^{2+}\text{Si})_{-1}$ exchange vectors (Fig. 7c). This representation illustrates the separation from zone-1 to zone-2 data reflecting the operation of the $(\text{TiR}^{2+})\text{Al}_{-1}$ exchange vector. Within each zone, the data are arrayed consistent with combinations of the $[\text{R}^{2+}(\text{OH})_2](\text{TiO}_2)_{-1}$ and $(\text{R}^{3+}\text{O})[\text{R}^{2+}(\text{OH})]_{-1}$ vectors. The Ti versus *W*-site O diagram also shows the separation of zone-1 relative to zone-2 data, consistent with the operation of the $(\text{TiR}^{2+})\text{Al}_{-1}$ exchange vector and supporting that correlation. These data suggest that the tourmaline compositions become more Ti-rich with less OH. However, the array of the zone-2 data appears most consistent with the $(\text{TiO}_2)[\text{R}^{2+}(\text{OH})_2]_{-1}$ vector suggesting a different mechanism of Ti incorporation. Operation of the $(\text{TiO}_2)[\text{R}^{2+}(\text{OH})_2]_{-1}$ vector to the point at which it reaches threshold values of $\text{Ti} > 0.25$ *apfu* and ${}^W\text{O} > 0.5$ for magnesian tourmalines marks the development of “magnesioutrowite” (Tab. 1). This hypothetical tourmaline species has also been described in the Zlatá Idka tourmalinites of Slovakia by Bačík et al. (2022).

5.3. Tourmaline element partitioning and constraints on metamorphic fluid compositions

The sulfate-rich meta-evaporite from Arignac allows examination of element partitioning among analyzed coexisting minerals in this relatively uncommon tourmaline-bearing lithology. Tourmaline, interpreted to have formed during peak metamorphism, has inclusions of scapolite and albite. In addition, coarser-grained, high-grade scapolite persists in the matrix. Assuming chemical equilibrium is approached, the Na–Ca partition coefficients ($K_D = (\text{Na}/\text{Ca})^{\text{tur}}/(\text{Na}/\text{Ca})^{\text{scp}}$) between the average zone-2 tourmaline composition (Tab. 2) versus the scapolite inclusions in zone-2 tourmaline, and the average matrix compositions of tourmaline and scapolite are 1.47 and 1.36, respectively. Similar Na–Ca tourmaline–scapolite partition coefficients (1.9–1.4) have been observed in amphibolite-facies plagioclase–muscovite–scapolite–tourmaline meta-

evaporite layers near Prosetín, Czech Republic (Bačík et al. 2012). This implies that tourmaline more effectively partitions Na relative to Ca than scapolite under these metamorphic conditions of formation.

In contrast, partitioning relations of Na–Ca tourmaline–plagioclase and scapolite–plagioclase in these samples are indicative of chemical disequilibrium. Plagioclase from replacement assemblages after scapolite as well as inclusions in tourmaline are all highly albitic, i.e., Ab > 98 % (Tab. 4). High-grade scapolite matrix and inclusion grains contain a substantial amount of Ca (11–27 % Me component). Where the matrix scapolite is partially pseudomorphed (Fig. 3b), it has a local assemblage of albite ($\text{Ab}_{98.2}\text{An}_{0.2}\text{Or}_{1.6}$), K-feldspar ($\text{Ab}_{11.9}\text{An}_{0.1}\text{Or}_{88.0}$) and calcite (Tab. 4). Based on experimental scapolite–plagioclase stability relations (Almeida and Jenkins 2019), scapolite of those compositions found in the Arignac meta-evaporite should coexist with considerably more calcic plagioclase ($> \sim \text{An}_{10-20}$) for the assumed peak metamorphic conditions. Empirical and experimental tourmaline–plagioclase Na–Ca partitioning (van Hinsberg and Schumacher 2009; Dutrow and Henry 2018) shows that the $\text{Ca}/(\text{Ca} + \text{Na})$ ratio in tourmaline is roughly equivalent to that in the coexisting plagioclase. Therefore, the average zone-1 tourmaline should coexist with An_{35} plagioclase and zone-2 tourmaline should coexist with An_{23} plagioclase. This lack of coherency in the partitioning data further suggests the low(er)-temperature replacement of scapolite by albite of a dramatically different composition. The interpretation is that plagioclase has been reset to albitic compositions during the influx of low-grade fluids that locally accessed scapolite inclusions in tourmaline along fractures to alter their chemical composition (Fig. 4). As such, these minerals show chemical disequilibrium.

Experimental, theoretical, and empirical studies of tourmaline–aqueous fluid element partitioning permit quantitative estimates of specific fluid-phase components to be determined based on the tourmaline compositions (e.g., von Goerne et al. 2001, 2011; Berryman et al. 2015; 2016, 2017; Dutrow and Henry 2016, 2018; van Hinsberg et al. 2017). Dutrow and Henry (2016) fit the experimental data of Na and Ca occupancy of tourmaline *X*-site (von Goerne et al. 2011) to temperature-independent expressions that allow the Na and Ca concentration of coexisting aqueous fluids in equilibrium with intermediate Na–Ca tourmaline to be approximated. For the Arignac tourmaline, assuming 600 °C, these expressions yield estimates of $\text{Na}^+_{\text{fluid}}$ of 480 mM and $\text{Ca}^{2+}_{\text{fluid}}$ of 160 mM for average zone-1 and $\text{Na}^+_{\text{fluid}}$ of 460 mM and $\text{Ca}^{2+}_{\text{fluid}}$ of 110 mM for average zone-2. This can be compared to modern surface seawater with Na^+ of 481 mM and Ca^{2+} of 10.5 mM (Pilson 1998). Although the Na^+ concentration in the Arignac brine is comparable to that of seawater, the

Ca^{2+} concentration is more than ten times that of modern seawater, but more similar to concentrations in ancient seawater and basinal brines (Lowenstein et al. 2003; Hanor and McIntosh 2006). These data support the usual interpretation of higher salinity fluids typically found in association with tourmalines developed in (meta)-evaporites and the operation of the deprotonation vector $\text{AlO}[\text{Mg}(\text{OH})]_{-1}$ in these saline environments (e.g., Henry et al. 2008). Quantitative estimates of other components in aqueous fluids in equilibrium with tourmaline can be calculated from empirical tourmaline-fluid partitioning data using the empirical approach of van Hinsberg et al. (2017). Using the partition coefficients in conjunction with the average EMPA data, zone 1 and zone 2 of the Arignac tourmaline, the following concentrations for dissolved constituents of the coexisting aqueous fluid are estimated: 144.7 ppm B, 3.0 ppm Cr, 8.6 ppm Mn and 53.6 ppm Ti for zone 1; compared to 145.4 ppm B, 0.7 ppm Cr, 13.6 ppm Mn and 16.6 ppm Ti for zone 2. These calculated concentrations can be compared to modern surface seawater with B of 4.45 ppm, Cr of 0.0002 ppm, Mn of 0.0004 ppm and Ti of 0.001 ppm (Turekian 1968). Clearly, the high-temperature brines can accommodate greater concentra-

tions of dissolved constituents. Overall, an acidic, saline Na–B-rich fluid phase, implied by the tourmaline compositions, is consistent with the marialitic scapolite that develops at high grades in the Arignac sample.

5.4. Tourmaline in sulfate-bearing meta-evaporites and other meta-evaporites

Tourmaline data from the Arignac locality provide new data for lithological regions in the highly magnesian portion of the Al–Fe–Mg subsystem source-rock type diagram (Figs 1, 8). The Arignac data straddle the bound-

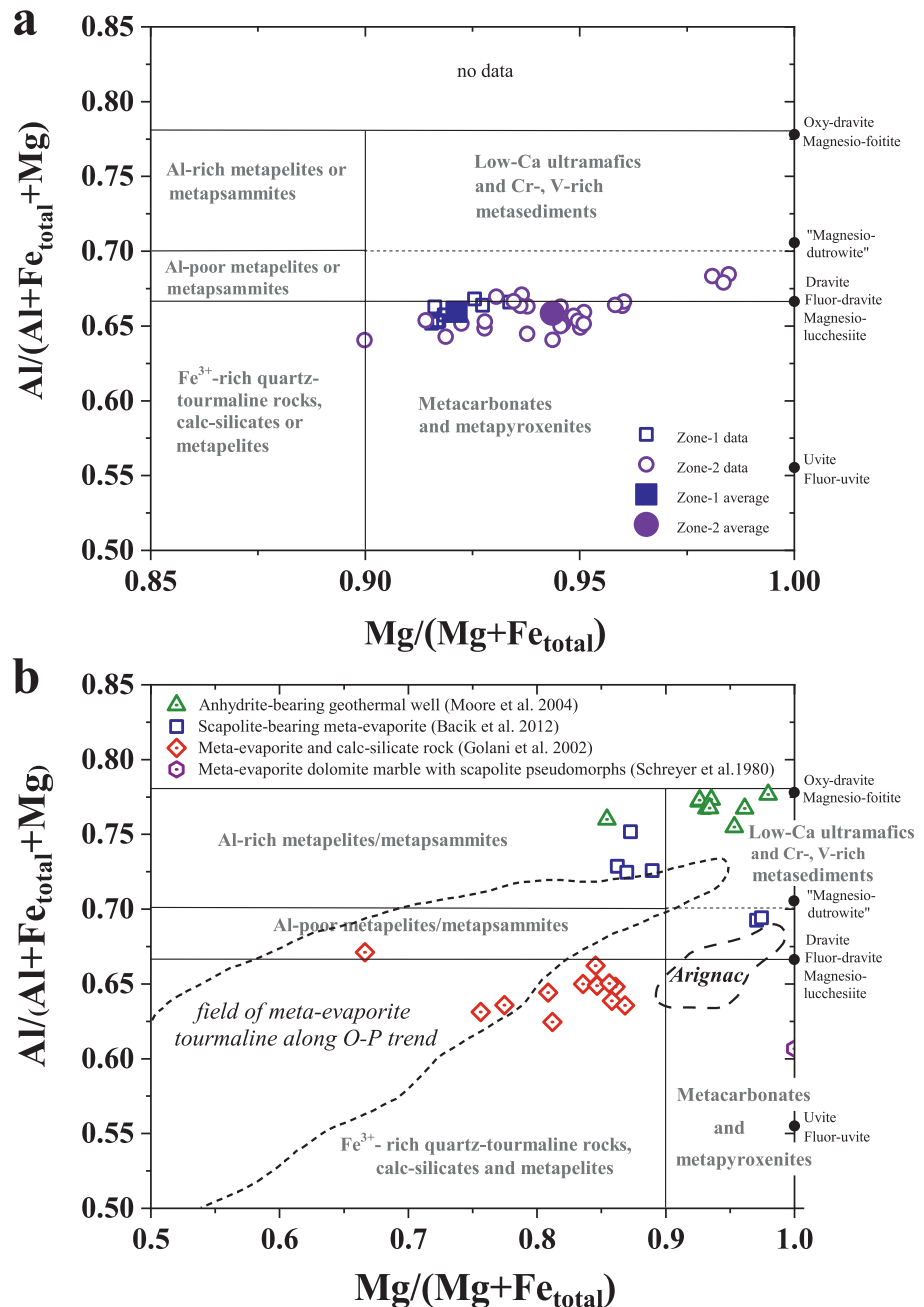


Fig. 8 Tourmaline data in the Mg-rich portion of the Al–Fe–Mg diagram showing tourmaline compositions and likely source-rock types (after Henry and Guidotti 1985 as modified by Henry and Dutrow 2018). **a** – Magnesian-rich portion of a diagram showing the zone-1 and zone-2 tourmaline compositions from the Arignac sample. All compositions are $> 0.9 X_{\text{Mg}}$. **b** – Magnesian portion of diagram with comparative tourmaline data. The long-dashed curve shows the compositional field of the Arignac meta-evaporite sample; the short-dashed curve represents the field associated with tourmalines originally defining the O–P trend (Henry et al. 2008). Additional tourmaline data are provided for tourmaline developed in an anhydrite-bearing active geothermal system (Moore et al. 2004), a medium-grade scapolite-bearing meta-evaporite (Bačík et al. 2012), a carbonate/tourmalinite meta-evaporite terrain (Golani et al. 2002) and a meta-evaporitic dolomitic marble (Schreyer et al. 1980).

ary among all the previously defined fields: the low-Ca ultramafics and Cr-, V-rich metasediments field; the Mg extension of the Al-poor metapelites and metapsammities field and the metacarbonates and metapyroxenites field (Fig. 8a). Clearly, additional fields need to be developed for sulfate-rich meta-evaporite lithologies on this source-rock diagram. Additionally, highly magnesium tourmalines may be indicators of these unusual (meta-) evaporitic environments.

Comparing the Arignac data to other meta-evaporites and sulfate- or scapolite-bearing lithologies highlights commonalities and differences of tourmaline compositions. (1) The Arignac tourmalines are similar in composition to the series of meta-evaporitic tourmaline compositions that were used to define the O–P trend; i.e., Fe is entirely or almost entirely Fe³⁺ and the W-site is commonly enriched in O or is O-dominant (see Henry et al. 2008). This continuous compositional O–P trend extends from Al-free povondraite to close to the oxy-dravite composition, generally following the Fe³⁺Al₁ exchange vector (Fig. 8b). However, the Arignac tourmaline is different in that it has, overall, higher Mg and Ca contents with Mg/(Mg + Fe_{total}) > 0.90 and Ca typically > 0.2 apfu. (2) A series of Proterozoic tourmaline-, phlogopite-, scapolite-bearing metamorphosed carbonate rocks with intercalated quartzofeldspathic lithologies are interpreted as hypersaline evaporitic metasediments associated with gold mineralization in NW India (Golani et al. 2002). Here, tourmaline compositions are mostly Ca-rich oxy-dravites but exhibit a range of compositions with Mg/(Mg + Fe_{total}) ratios extending from the O–P trend meta-evaporite field toward those of the Arignac field (Fig. 8b). (3) The Karaha–Telaga Bodas geothermal well, Indonesia, part of an active and young (4200 y BP) oxygenated, vapor-dominated hydrothermal system (Moore et al. 2004), contains sparse tourmaline. Tourmaline, encapsulated in anhydrite or quartz, is associated with fluorite and calcite, and appears to be a late feature of the hydrothermal–volcanic system. Fluid inclusions in anhydrite suggest temperatures were ~190 °C with salinities of 2.7–3.4 wt. % NaCl or H₂SO₄ equivalent during quartz, anhydrite, and tourmaline formation. Tourmaline analyses from a single sample show that they are aluminous and magnesian (Mg/(Mg + Fe_{total}) > 0.85), have substantial X-site vacancy and are all oxy-dravites (Fig. 8b). Relative to the Arignac tourmaline, the geothermal tourmaline is more aluminous with high X-site vacancy, close to the oxy-dravite/magnesio-foitite point on the AFM diagram. (4) Magnesian tourmaline from plagioclase-muscovite-scapolite meta-evaporite layers in dolomite marble near Prosetín, Czech Republic form three compositional types within single, zoned tourmalines and range from dravites to oxy-dravites (Bačík et al. 2012). The

marbles are estimated to have developed at 500–600 °C and 5 kbar. Tourmaline compositional zoning, related to prograde growth, becomes more magnesian (Mg/(Mg + Fe_{total}) = 0.86–0.97) and calcic (Ca = 0.02–0.29 apfu). The outermost compositional type mimics that of the Arignac tourmalines (Fig. 8b). (5) Tourmaline in a dolomitic marble, interpreted as a meta-evaporite sequence, has an assemblage of dolomite – albite (An_{2–3}) – Na-phlogopite–talc–tourmaline–quartz–rutile–pyrite (Schreyer et al. 1980). The estimated conditions of metamorphism is < 400 °C and 2–3 kbar at low X(H₂O) and high X(CO₂). The tourmaline in the meta-evaporite is a dravite with a significant uvite component (although F was not analyzed) more similar to typical meta-carbonate tourmaline (e.g., Henry and Guidotti 1985).

6. Conclusions

Tourmaline and associated mineral-inclusion chemical data provide important dimensions to delineate formation conditions in rocks that are deformed, infiltrated by fluids and thermally retrogressed. Further, tourmaline may be the only residual trace of the prior high-grade metamorphic mineral assemblage to form in these environments. This is the case for the unusual assemblage of anhydrite and gypsum, together with tourmaline, in the sulfate-rich meta-evaporite of the Arignac locality, thereby providing new data for tourmaline formation in these uncommon environments. Their highly magnesian compositions contribute to our understanding of Mg-rich tourmaline formation and coexisting fluid compositions, require a modification of the AFM host rock compositional fields, and underscore the breadth of environments in which tourmaline forms.

Acknowledgments We thank Dr. Matthew Loocke for assisting with the electron microprobe analyses, imaging, and polishing. Appreciation is due to the discerning eye of Alfredo Petrov, who led Dutrow to this unique tourmaline find at the Tucson mineral show, Dr. Eloïse Gaillou, who generously located additional locality information, and to Dr. Jeff Hanor, who provided guidance on fluid chemistries. The authors acknowledge their LSU professorships for partial funding; Campanile Charities (DJH) and Adolphe G. Gueymard (BLD). Portions of this study benefited from National Science Foundation funding to BD and DH (grant number EAR-1551434). The authors are grateful to Vincent van Hinsberg, who always asks hard questions, and Peter Bačík for their insightful reviews, as well as to Jan Cempírek for his excellent handling of the manuscript as associate editor.

Electronic supplementary material. Complete quantitative electron microprobe data for Ca-rich tourmaline, scapo-

lite and plagioclase are available online on the Journal website (<http://dx.doi.org/10.3190/jgeosci.352>).

References

- ADLAKHA EE, HATTORI K (2016) Paragenesis and composition of tourmaline types along the P2 Fault and McArthur River Uranium Deposit, Athabasca Basin, Canada. *Canad Mineral* 54: 661–679
- ALEKSANDROV SM, TRONEVA MA (2006) Composition, mineral assemblages, and genesis of serendibite-bearing magnesian skarns. *Geochem Int* 44: 665–680
- ALMEIDA KMF, JENKINS DM (2019) A comparison between the stability fields of a Cl-rich scapolite and the end-member marialite. *Amer Miner* 104: 1788–1799
- ARIF M, HENRY DJ, MOON CJ (2010) Cr-bearing tourmaline associated with emerald deposits from Swat, NW Pakistan: Genesis and its exploration significance. *Amer Miner* 95: 799–809
- AYUSO RA, BROWN CE (1984) Manganese-rich red tourmaline from the Fowler Talc Belt, New-York. *Canad Mineral* 22: 327–331
- BARBOSA, CP, FALSTER, AU, SIMMONS, WB, WEBBER, KL, NIZAMOFF, J GAINES, RV (2000) Minerals of the Brumado magnesite deposits, Serra das Eguas, Bahia, Brazil. *Rocks Miner* 75: 32–39
- BAČÍK P, MÉRES S, UHER P (2011) Vanadium-bearing tourmaline in metacherts from Chvojnica, Slovak Republic: Crystal chemistry and multistage evolution. *Canad Mineral* 49: 195–206
- BAČÍK P, UHER P, CEMPÍREK J, VACULOVÍČ T (2012) Magnesian tourmalines from plagioclase–muscovite–scapolite metaevaporite layers in dolomite marble near Prosetín (Olešnice Unit, Moravicum, Czech Republic). *J Geosci* 57: 143–153
- BAČÍK P, OZDÍN D, UHER, P, CHOVAN, M. (2022) Crystal chemistry and evolution of tourmaline in tourmaline-rich rocks from Zlatá Idka, Slovakia. *J Geosci* 67: 209–222
- BELLEY PM, GRICE JD, FAYEK M, KOWALSKI PM, GREW ES (2014) A new occurrence of the borosilicate serendibite in tourmaline-bearing calc-silicate rocks, Portage-du-Fort Marble, Grenville Province, Quebec; evolution of boron isotope and tourmaline compositions in a metamorphic context. *Canad Mineral* 52: 595–616
- BENISEK A, KROLL H, CEMIC L (2004) New developments in two-feldspar thermometry. *Amer Miner* 89: 1496–1504
- BENISEK A, DACHS E, KROLL H (2010) A ternary feldspar-mixing model based on calorimetric data: development and application. *Contrib Mineral Petrol* 160: 327–337
- BERRYMAN E, WUNDER B, WIRTH R, RHEDE D, SCHETTLER G, FRANZ G, HEINRICH W (2015) An experimental study on K and Na incorporation in dravitic tourmaline and insight into the origin of diamondiferous tourmaline from the Kokchetav Massif, Kazakhstan. *Contrib Mineral Petrol* 169: 1–16
- BERRYMAN EJ, WUNDER B, RHEDE D, SCHETTLER G, FRANZ G, HEINRICH W (2016) P–T–X controls on Ca and Na distribution between Mg–Al tourmaline and fluid. *Contrib Mineral Petrol* 171: 31
- BERRYMAN EJ, KUTZSCHBACH M, TRUMBULL RB, MEIXNER A, VAN HINSBERG V, KASEMANN SA, FRANZ G (2017) Tourmaline as a petrogenetic indicator in the Pfisch Formation, Western Tauern Window, Eastern Alps. *Lithos* 284–285: 138–155
- BUCHER K, GRAPES R (2011) Metamorphism of dolomites and limestones. In: *Petrogenesis of Metamorphic Rocks*, vol. Springer Berlin Heidelberg, Berlin, Heidelberg, pp 191–224
- CLERC C, LAHFID A, MONIÉ P, LAGABRIELLE Y, CHOPIN C, POUJOL M, BOULVAIS P, RINGENBACH JC, MASINI E, DE ST BLANQUAT M (2015) High-temperature metamorphism during extreme thinning of the continental crust: a reappraisal of the North Pyrenean passive paleomargin. *Solid Earth* 6: 643–668
- DAI Z, KAN AT, SHI W, ZHANG N, ZHANG F, YAN F, BHANDARI N, ZHANG Z, LUI L, RUAN G, TOMSON G (2017) Solubility measurements and predictions of gypsum, anhydrite and calcite over wide ranges of temperature, pressure and ionic strength with mixed electrolytes. *Rock Mech Rock Eng* 50: 327–339
- DESCOUENS D (1984) Les Mines de gypse d'Arnavé et Arignac. *Monde et Minéraux* 62:16–17
- DUTROW BL, HENRY DJ (2011) Tourmaline: A geologic DVD. *Elements* 7: 301–306
- DUTROW BL, HENRY DJ (2016) Fibrous tourmaline: A sensitive probe of fluid compositions and petrologic environments. *Canad Mineral* 54: 311–335
- DUTROW BL, HENRY DJ (2018) Tourmaline compositions and textures: reflections of the fluid phase. *J Geosci* 63: 99–110
- DUTROW BL, HENRY DJ (2021) Petrogenetic utility of magnesian tourmaline: extraordinary origin of everyday tourmaline. *Natura* 111: 29–30
- DUTROW BL, HENRY DJ, SUN Z (2019) Origin of corundum–tourmaline–phlogopite rocks from Badakhshan, northeastern Afghanistan: a new type of metasomatism associated with sapphire formation. *Eur J Mineral* 31: 739–753
- GOLANI PR, PANDIT MK, SIAL AN, FALLICK AE, FERREIRA VP, ROY AB (2002) B–Na-rich Palaeoproterozoic Aravalli metasediments of evaporitic association, NW India: A new repository of gold mineralization. *Precambrian Res* 116: 183–198
- GOLBERG JM, LEYRELOUP AF (1990) High temperature-low pressure Cretaceous metamorphism related to crustal thinning (Eastern North Pyrenean Zone, France). *Contrib Mineral Petrol* 104: 194–207

- HANOR JS, MCINTOSH JC (2006) Are secular variations in seawater chemistry reflected in the compositions of basinal brines? *J Geochem Explor* 89: 153–156
- HENRY DJ, DE BRODTKORB MK (2009) Mineral chemistry and chemical zoning in tourmalines, Pampa del Tamboreo, San Luis, Argentina. *J South Amer Earth Sci* 28: 132–141
- HENRY DJ, DUTROW BL (1990) Ca substitution in Li-poor aluminous tourmaline. *Canad Mineral* 28: 111–124
- HENRY DJ, DUTROW BL (1996) Metamorphic tourmaline and its petrologic applications. In: GREW ES, ANOVITZ LM (eds) *Boron: mineralogy, petrology and geochemistry*. *Rev Mineral Geochem* 33: 503–557
- HENRY DJ, DUTROW BL (2001) Compositional zoning and element partitioning in nickeloan tourmaline from a metamorphosed karstbauxite from Samos, Greece. *Amer Miner* 86: 1130–1142
- HENRY DJ, DUTROW BL (2012) Tourmaline at diagenetic to low-grade metamorphic conditions: Its petrologic applicability. *Lithos* 154: 16–32
- HENRY DJ, DUTROW BL (2018) Tourmaline studies through time: contributions to scientific advancements. *J Geosci* 63: 77–98
- HENRY DJ, DUTROW BL (2021) Tourmaline crystallography, crystal chemistry and nomenclature: current status. *Natura* 111: 47–48
- HENRY DJ, GUIDOTTI CV (1985) Tourmaline as a petrogenetic indicator mineral: an example from the staurolite-grade metapelites of NW Maine. *Amer Miner* 70: 1–15
- HENRY DJ, KIRKLAND BL, KIRKLAND DW (1999) Sector-zoned tourmaline from the cap rock of a salt dome. *Eur J Mineral* 11: 263–280
- HENRY DJ, DUTROW BL, SELVERSTONE J (2002) Compositional polarity in replacement tourmaline – an example from the Tauern Window, eastern Alps. *Geol Mater Res* 4: 1–23 (abstract referenced in *Amer Miner*, 88, 1399)
- HENRY DJ, SUN H, SLACK JF, DUTROW BL (2008) Tourmaline in meta-evaporites and highly magnesian rocks; perspectives from Namibian tourmalinites. *Eur J Mineral* 20: 889–904
- HENRY DJ, NOVÁK M, HAWTHORNE FC, ERTL A, DUTROW BL, UHER P, PEZZOTTA F (2011) Nomenclature of the tourmaline-supergrout minerals. *Amer Miner* 96: 895–913
- KOSZTOLANYI C, MULLIS J, WEIDMANN M (1987) Measurements of the phase transformation temperature of gypsum-anhydrite, included in quartz, by microthermometry and Raman microprobe techniques. *Chem Geol* 61: 19–28
- LAGABRIELLE Y, LABAUME P, DE SAINT BLANQUAT M (2010) Mantle exhumation, crustal denudation, and gravity tectonics during Cretaceous rifting in the Pyrenean realm (SW Europe): Insights from the geological setting of the lherzolite bodies. *Tectonics* 29(4)
- LAGABRIELLE Y, ASTI R, DURETZ T, CLERC C, FOURCADE S, TEIXELL A, LABAUME P, CORRE B, SASPITURRY N (2020) A review of cretaceous smooth-slopes extensional basins along the Iberia-Eurasia plate boundary: How pre-rift salt controls the modes of continental rifting and mantle exhumation. *Earth Sci Rev* 201: 103071
- LOWENSTEIN TK, HARDIE LA, TIMOFEEFF MN, DEMICCO RV (2003) Secular variation in seawater chemistry and the origin of calcium chloride basinal brines. *Geol* 31, 857–860
- MARGER K, LUISIER C, BAUMGARTNER LP, PUTLITZ B, DUTROW BL, BOUVIER A-S, DINI A (2019) Origin of Monte Rosa whiteschist from in-situ tourmaline and quartz oxygen isotope analysis by SIMS using new tourmaline reference materials. *Amer Miner* 104: 1503–1520
- Mindat website. <https://www.mindat.org/loc-67479.html> (last accessed December 23, 2021)
- MODRESKI PJ, FOORD EE, BARBOSA CP (1997) Crystal chemistry of uvite-dravite from the Brumado magnesite deposits, Bahia, Brazil. In: *Tourmaline 1997 International Symposium on Tourmaline, Abstract Volume*, 59–60
- MOORE JN, CHRISTENSON BW, ALLIS RG, BROWNE PRL, LUTZ SJ (2004) The mineralogical consequences and behavior of descending acid-sulfate waters: An example from the Karaha–Telaga Bodas geothermal system, Indonesia. *Canad Mineral* 42: 1483–1499
- PERTLIK F, ERTL A, KORNER W, BRANDSTATTER F, SCHUSTER R (2003) Na-rich dravite in the marbles from Friesach, Carinthia, Austria: Chemistry and crystal structure. *Neu Jb Mineral Mh*: 277–288
- PESQUERA A, GIL-CRESPO PP, TORRES-RUIZ F, TORRES-RUIZ J, RODA-ROBLES E (2016) A multiple regression method for estimating Li in tourmaline from electron microprobe analyses. *Mineral Mag* 80: 1129–1133
- PILSON MEQ (1998) *An Introduction to the Chemistry of the Sea*. Prentice Hall, pp 1–431
- PUTIRKA KD (2008) Thermometers and barometers for volcanic systems. *Rev Mineral Geochem* 69: 61–120
- RIEHL, W, CABRAL, A.R. (2018) Meta-evaporite in the Carajás mineral province, northern Brazil. *Miner Depos* 55: 895–902
- SCHERTL HP, SCHREYER W, CHOPIN C (1991) The pyrope-coesite rocks and their country rocks at Parigi, Dora Maira Massif, Western Alps – Detailed petrography, mineral chemistry and PT path. *Contrib Mineral Petrol* 108: 1–21
- SCHREIBER BC, HELMAN ML (2005) Criteria for distinguishing primary evaporite features from deformation features in sulfate evaporites. *J Sediment Res* 75: 525–533
- SCHREYER W, ABRAHAM K (1976) Three-stage metamorphic history of a whiteschist from Sar e Sang, Afghanistan, as part of a former evaporite deposit. *Contrib Mineral Petrol* 59: 111–130
- SCHREYER W, ABRAHAM K, KULKE H (1980) Natural sodium phlogopite coexisting with potassium phlogopite and sodian aluminian talc in a metamorphic evaporite sequence

- from Derrag, Tell Atlas, Algeria. *Contrib Mineral Petrol* 74: 223–233
- SLACK JF, HERRIMAN N, BARNES RG, PLIMER, IR (1984) Stratiform tourmalinites in metamorphic terranes and their geologic significance. *Geol* 12, 713–716
- THIÉBAUT J, DURAND-WACKENHEIM C, DEBEAUX M, SOUQUET P (1992) Métamorphisme des évaporites triasiques du versant nord des Pyrénées centrales et occidentales. *Bull Soc hist nat Toulouse* 128: 77–84
- TUREKIAN, KK (1968) *Oceans*. Prentice-Hall, pp 1–120
- WARREN JK (2016) Meta-evaporites. In: *Evaporites: A Geological Compendium*. vol. Springer International Publishing, Cham, pp 1375–1468
- UHER P, JANÁK M, OZDÍN D (2002) Calcian dravite from metacarbonate rocks of the Mutník magnesite–talc deposit, Hnusta, Slovakia. *Neu Jb Mineral Mh*: 68–84
- VAN HINSBERG VJ, SCHUMACHER JC (2009) The geothermobarometric potential of tourmaline, based on experimental and natural data. *Amer Miner* 94: 761–770
- VAN HINSBERG VJ, HENRY DJ, DUTROW BL (2011a) Tourmaline as a petrologic forensic mineral: A unique recorder of its geologic past. *Elements* 7: 327–332
- VAN HINSBERG VJ, HENRY DJ, MARSCHALL HR (2011b) Tourmaline: An ideal indicator of its host environment. *Canad Mineral* 49: 1–16
- VAN HINSBERG VJ, FRANZ G, WOOD BJ (2017) Determining subduction-zone fluid composition using a tourmaline mineral probe. *Geochem Perspect Lett* 3: 160–169
- VANKO DA, BISHOP FC (1982) Occurrence and origin of marialitic scapolite in the Humboldt Lopolith, NW Nevada. *Contrib Mineral Petrol* 81: 277–289
- VON GOERNE G, FRANZ G, HEINRICH W (2001) Synthesis of tourmaline solid solutions in the system Na_2O – MgO – Al_2O_3 – SiO_2 – B_2O_3 – H_2O – HCl and the distribution of Na between tourmaline and fluid at 300 to 700 °C and 200 MPa. *Contrib Mineral Petrol* 141: 160–173
- VON GOERNE G, FRANZ G, VAN HINSBERG VJ (2011) Experimental determination of Na–Ca distribution between tourmaline and fluid in the system CaO – Na_2O – MgO – Al_2O_3 – SiO_2 – B_2O_3 – H_2O . *Canad Mineral* 49: 137–152
- YAMAMOTO H, KENNEDY GC (1969) Stability relations in the system CaSO_4 – H_2O at high temperatures and pressures. *Amer J Sci* 267-A: 550–557

